Check for updates

Architectural View of Flexible Aliphatic –OH Group Coordinated Hemi-Directed Pb(II)-Salen Coordination Polymer: Synthesis, Crystal Structure, Spectroscopic Insights, Supramolecular Topographies, and DFT Perspective

Dhrubajyoti Majumdar[1,2] · Burak Tüzün[3] · Tapan Kumar Pal[4] · Sourav Das[5] · Kalipada Bankura[1]

Abstract

We serendipitously designed one novel 1D hetero-binuclear Zn(II)-Pb(II) coordination polymer, namely $[(Zn)(Pb)(L)(\eta^1-NCS)(\eta^1-SCN)]_n$ (1) from Salen ligand (H_3L) in the presence of NaSCN. The complex was structurally characterized by elemental, IR, Raman, NMR spectroscopy, Scanning electron microscope, Powder X-ray diffraction, and Single-crystal X-ray diffraction (SCXRD). The heteronuclear complex crystallizes in the monoclinic space group P21/c with Z=4. The asymmetric unit contains one deprotonated ligand (L^{2-}). SCXRD comprises metal ions of Zn(II) and Pb(II), fulfiled perfect square bipyramidal and Hemi-directed coordination spheres. We accomplished DFT by three different level basis set B3LYP, HF, and M062X with Lanl2dz to delineate Frontier molecular orbital, the Global chemical parameters, and the molecular electrostatic potential. Hirshfeld surface carried out non-covalent interactions like hydrogen bonding. This bonding considered the possible supramolecular topographies due to the flexible aliphatic –OH group. Besides H/H, C/H/H/C and N/H/H/N also dominated the supramolecular network. Van der Waals interactions appear to be more prevalent in the molecular packaging of the complex. Molecular docking finds the plausible binding process by implanting the complex into the active site of the crystal structures of estrogen receptor protein, the VEGFR kinase (liver cancer) protein, and the allosteric Eya2 phosphatase inhibitor (lung cancer) protein. The essential binding process is the polar and hydrophobic exchanges, π–π interaction, hydrogen bonds, and halogen. Advanced Protein–Ligand Interaction Profiler crucially examined the interplay of the protein with complex. Finally, NLO parameters polarizability (α) and hyperpolarizability (β) calculated the importance of nonlinear optical effects.

✉ Dhrubajyoti Majumdar
dmajumdar30@gmail.com

✉ Kalipada Bankura
kalipada2010@gmail.com

1   Department of Chemistry, Tamralipta Mahavidyalaya, Tamluk, West Bengal 721636, India

2   Department of Chemistry, Indian Institute of Technology (Indian School of Mines), Dhanbad, Jharkhand 826004, India

3   Department of Plant and Animal Production, Sivas Vocational School, Sivas Cumhuriyet University, 58140 Sivas, Turkey

4   Department of Chemistry, Pandit Deendayal Petroleum University, Gandhinagar 382007, India

5   Department of Basic Sciences, Chemistry Discipline, Institute of Infrastructure Technology Research and Management, Near Khokhara Circle, Maninagar East, Ahmedabad, Gujarat 380026, India

Graphical Abstract
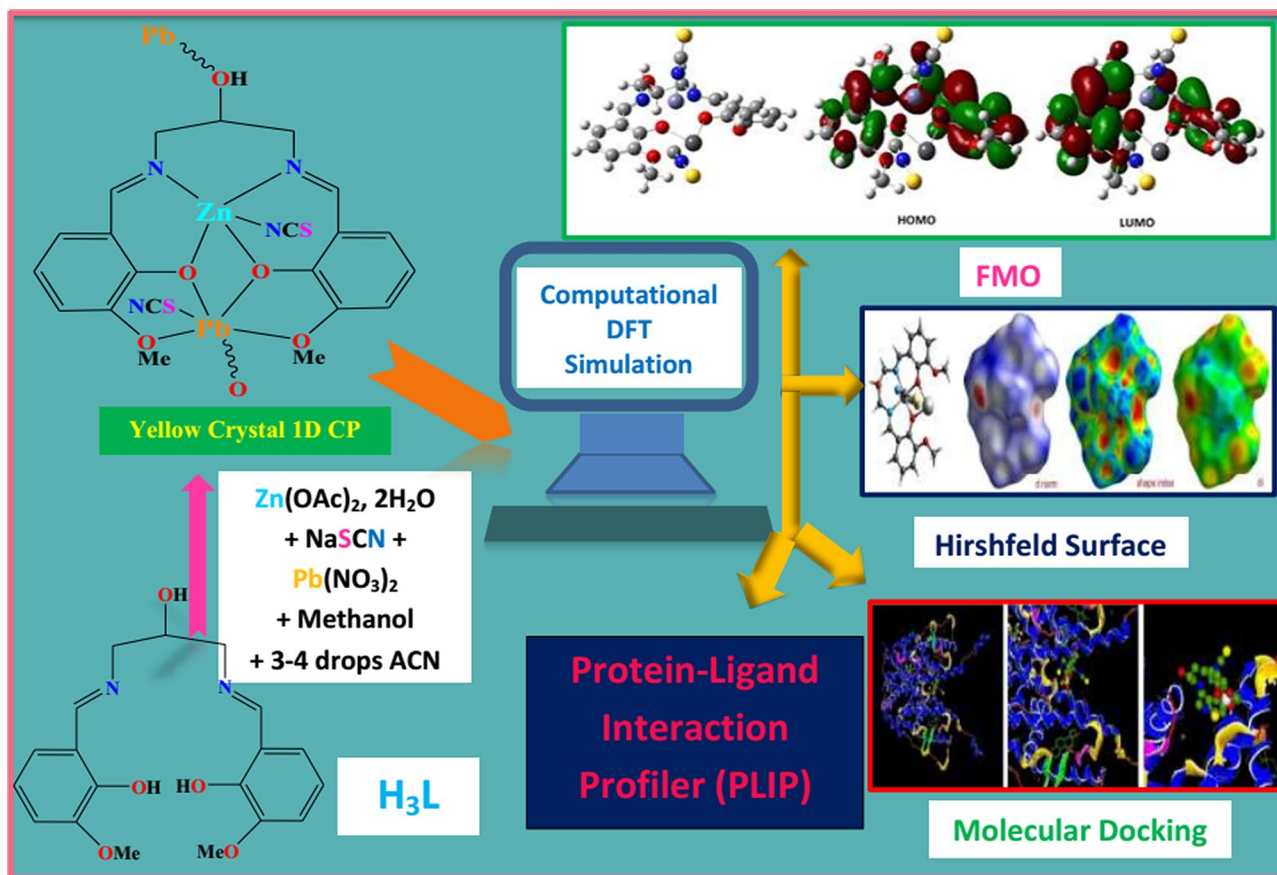
Keywords Salen ligand · Heterobimetallic complex · DFT · Molecular docking · PLIP

1 Introduction

The synthesis of coordination polymers (CPs) has attracted significant research contributions in the prevalent research scenario. The aesthetic, structural topologies [1] motivated the young synthetic chemists to explore their research into CPs, which may be homo/heterometallic. Most of the CPs have global applications like gas storage and separation [2], nonlinear optics [3, 4], magnetism [5, 6], luminescence [7], sensing [8, 9], catalysis [10, 11], energy storage [12–15] and host–guest chemistry [16–18]. The design of self-assemblies through cooperative interactions, such as strong/weak hydrogen bonding, C–H–π and π–π stacking regulate the structure, and dimensionality CPs are another milestone in research [19–21]. The directional metal–ligand potent bonds, d^{10}–d^{10} (aurophilic/argentophilic) interactions also sustain supramolecular solid-state architectures [22]. The choice of metal ions, the ligand, the solvent, pH, node, and spacers like Thiocyanate, Azide, Dicyanamide, etc., influence the novel CPs design [23–27]. Interestingly, Salen ligands derived from

the condensation between diamines and substituted *ortho* vanillin are possibly considered bicompartmental. Herein two substantially different coordination pockets, an inner tetradentate planar compartment involving imine N_2 and phenoxy-O_2 (Scheme S1). In contrast, the outer pocket consists of O_4 atoms, two from phenoxy and methoxy units. A 3d metal ion prefers the inner N_2O_2 compartment, while the larger open O_4 coordination pocket for s, p, and f-block metal ions [28–36] (Scheme S2A). As part of the prescribed research, we envisioned the introduction of a Flexible aliphatic –OH group into the Salen (Scheme S2B). Such a category enhances the ability of the heteronuclear CPs to hydrogen bond after the coordination of Pb(II) ions. Such an implication changes the supramolecular crystal structures and the dimensionality of the resulting solids. In the meantime, in addition to the change in size and charge of new metal ions, a wide range of CPs [37] in the relevant systems can offer components for H-bonds. Many supramolecular aggregates can therefore be expected [38–41]. Here, too, the coordination chemistry of Pb(II) is not inviolable. The

present study on the synthesis of Ni(II)/Pb(II) complexes inspires our Scholars to quest for new CPs of Pb(II)-Salen, particularly concerning the existence of thiocyanate linkers (Scheme S3) [25]. The high atomic number ($Z = 82$) and radius factor are sufficient to embrace other coordination numbers variation from 2 to 10 to proceed in variable valence states. These skillful factors attracted synthetic inorganic chemists to map distinctive lead complexes [42–45]. Pb is lethal [46] subsequently must embrace good safe concerning synthesizing its complexes. Lead materials are popularly exploited in semiconductors, batteries, ferroelectric, and nonlinear optical [47–49]. Remarkably, two different structural organizations characterize the Lead Tetrel bonding [50, 51]. The electronic configuration $[Xe]4f^{14}5d^{10}6s^{2}6p^{2}$ of Pb makes inadequate screening of $4f^{14}$ and $3d^{10}$ electrons produce the $6s^{2}$ electron pair inert. The high penetration of the 6 s orbital and the relativistic stabilization of $6s^{2}$ electrons are necessary for the inert pair effect [52–54]. However, lone pair of Pb is stereo-dynamic and inactive in a few of the complexes, attending to drive Hemi-directional [55, 56] or Holo-directed complexes (Scheme S4) [46, 57]. Meanwhile, all zinc metal complexes with a CFSE value zero in the ground states, which is primordial for other d^{n} electronic systems (n = number of d orbital electrons) [58], favor the achievement of a variable stereochemistry. Computer-assisted DFT calculations are a technique used to compare the activities of the as-synthesized compounds [59, 60]. The HOMO–LUMO's energy gap, HS, and MEP perceived the metal complexes as unconventional reactivity [61, 62]. NLO of the metal complex boosts the nonlinear optical effect [63]. PLIP and MD experiments successfully combine the novel compound's experimental and theoretical biological activities [64].

Keeping all these aspects in mind, we report here on the synthesis, characterization, crystal structure, and supramolecular topologies of a novel CP, $[(Zn)(Pb)(L)(\eta^{1}\text{-}NCS)(\eta^{1}\text{-}SCN)]_{n}$ (**1**) realized from one flexible aliphatic –OH group pendant ligand. Exciting computational experiments MD, PLIP, and NLO were also carried over to the coordination polymer.

2 Experimental

2.1 Synthetic Materials

All research chemicals and solvents used to synthesize ligand and the complex were reagents graded without further purification. $Zn(OAc)_{2}\cdot 2H_{2}O$, $Pb(NO_{3})_{2}$, Sodium thiocyanate (NaSCN), 3-methoxy-2-hydroxybenzaldehyde, 2-hydroxy-1,3-diaminopropane were purchased from the Sigma Aldrich Company, USA. All the synthetic chemicals are GR quality.

2.2 Physical Measurements

Common elemental (CHN) analyses were completed on a PerkinElmer 2400 elemental analyzer. IR and Raman spectra were recorded as KBr pellets (4000–400 cm^{-1}) using a Perkin–Elmer spectrum RX 1 and BRUKER RFS 27 (4000–50 cm^{-1}) model. ^{1}H and ^{13}C NMR spectra were collected on a Bruker 400 MHz and 75.45 MHz FT-NMR spectrometer operating tetramethylsilane (TMS) as an internal standard in DMSO-d$_{6}$. BRUKER AXS performed powder X-ray diffraction (PXRD) measurements and the GERMANY X-ray diffractometer D8 FOCUS model using Cu Kα-1 radiation. UV–Visible spectra of ligand (CH$_{3}$OH) and the complex (DMSO) (200–1100 nm) were determined using the Hitachi model U-3501 spectrophotometer.

2.3 DFT Methodology

Theoretical studies are potentially considered to compare the chemical and biological activities of the heteronuclear metal complex. With theoretical studies, it is possible to obtain more effective and more active molecules. For these calculations, optimized structures were obtained using the Gaussian software program [65]. Many quanta chemical parameters have been obtained employing complex optimized structures. Parameters such as E_{HOMO}, E_{LUMO}, ΔE (HOMO–LUMO energy gap), chemical hardness (η), chemical potential (μ), nucleophilicity (ε), electronegativity (χ), electrophilicity (ω), and global softness (σ), are calculated because of DFT calculations [66, 67]. Each calculated parameter provides important information about the studied metal complex. NLO (non-linear optical) properties of the metal complex will be examined. HS analysis was performed for active site analysis. Then, the biological activities of the molecule against cancer proteins were compared. The proteins and metal complex files were studied at HEX 8.0.0 programs [68]. For molecular docking calculation purposes, the crystal structure of estrogen receptor protein, the crystal structure of VEGFR kinase (liver cancer) protein, and the crystal structure of an allosteric Eya2 phosphatase inhibitor (lung cancer) protein were used. The following parameters are used for docking: correlation type shape only, FFT mode: 3D, grid dimension: 0.6, receptor range: 180, ligand range: 180, twist range: 360, distance range: 40. Finally, Protein–Ligand Interaction Profiler (PLIP) server was used to examine the interaction between protein and the metal complex [69, 70].

2.4 X-Ray Crystallographic Data Collection and Refinement

Yellow crystal complexes were grown after slow evaporation of the methanol solvent in the existence of a few

drops of acetonitrile. We have selected good quality 3–4 crystals with microscopic observance for crystal data processing purposes. The crystal data have been collected on a Bruker CCD [71] diffractometer using Mo Kα radiation at $\lambda = 0.71073$ Å. We have used a few different popular crystallographic programs: *SMART* used for accumulating frames of information, indexing reflections, and determining lattice parameters, *SAINT* [72] for the combination of the intensity of reflections, and scaling, *SADAB* [73] for absorption correction, and *SHELXTL* for space group, structure determination, and least-squares refinements on *F2*. The crystal structure was solved utilizing full-matrix least-squares methods against *F2* using *SHELXL*-2014 [74] and *Olex-2* software [75]. All the non-H atoms had been refined with anisotropic displacement parameters, and all hydrogen positions were constant at calculated positions, which can be delicate isotropically. An outline of crystallographic information and complete structure refinement parameters are presented in Table 1.

2.5 Synthesis of Salen Ligand (H₃L)

The ligand has been synthesized following the literature method after slight modification (Scheme 1) [76]. The reflux condensation of 3-methoxy-2-hydroxybenzaldehyde (0.1522 g, 1 mmol) with 2-hydroxy-1,3-diaminopropane (0.0451 g, 0.5 mmol) in (50 mL) methanol at 60 °C for 3 hr prepared H_3L. Under vacuum, the solvent was removed, and the yellow solid product separated upon cooling, and the product was air-dried. Yield: 0.212 g (85.2%), Anal. Calc. for $C_{19}H_{22}N_2O_5$: C, 63.67; H, 6.19; N, 7.82 Found: C, 63.62; H, 6.24; N, 7.84%. IR (KBr cm⁻¹) selected bands: ν(C=N), 1661 vs, ν(C–O$_{phenolic}$) 1239 vs, ν(O–H) 3216 m, ¹H NMR (DMSO-d6, 400 MHz): δ (ppm): 3.83–3.86 (s, 3H¹), 4.08 (1H, aliphatic –OH⁸), 7.37–7.38 (m, 1H²–H⁴), 8.65 (m, 1H⁶), 13.91 (m,1H⁵), 3.32–3.77 (s, 2H⁷), (Scheme S5), ¹³C NMR (DMSO-d6, 75.45 MHz): δ (ppm): 55.19–67.69 (O–¹CH₃), 106.12–132.93 (Arom–³C–⁵C), 152.26 (⁷C–OH), 168.40–172.62 (⁸CH=N), UV–Vis λ_{max} (CH₃OH): 341, and 425 nm.

## 2.6 Synthesis of [(Zn)(Pb)(L)(η¹-NCS)(η¹-SCN)]ₙ (1)

Zinc acetate dihydrate (0.219 g, 1 mmol) was dissolved in 25 mL of hot methanol. Then a methanolic solution of H_3L (0.359 g, 1 mmol) was added, followed by the drop-wise inclusion of an aqueous methanolic solution of NaSCN (0.0811 g, 1 mmol). The resultant mixture refluxed for 3 hr at room temperature. 10 mL methanol solution of Pb(NO₃)₂ (0.331 g, 1 mmol) and 5–6 drops of acetonitrile (ACN) were

Table 1 Crystal data and structure refinement parameters

Formula	$C_{21}H_{20}N_4O_5PbS_2Zn$
M/g	745.09
Crystal system	Monoclinic
Space group	*P 1 21/c 1*
a/Å	9.813(7)
b/Å	16.798(12)
c/Å	15.066(11)
α (°)	90
β (°)	97.022(9)
V/Å³	2465(3)
Z	4
ρ_c/gcm⁻³	2.008
μ/mm⁻¹	8.004
F (000)	1432
θ range (deg)	2.42 to 17.41
Limiting indices	− 11 ≤ h ≤ 11 − 20 ≤ k ≤ 20 − 18 ≤ l ≤ 18
Reflns collected	59,792
Ind reflns	4584 [R_{int} = 0.1269, $Rsigma$ = 0.0565]
Completeness to θ (%)	0.999
Refinement method	Full-matrix-block least-squares on F²
Data/restraints/ parameters	4584/0/310
Goodness-of-fit on F^2	1.030
Final R indices [$I > 2\sigma(I)$]	R_1 = 0.0832 wR_2 = 0.2458
R indices (all data)	R_1 = 0.1099 wR_2 = 0.2761
Largest diff. peak and hole(e·Å⁻³)	6.240 and − 2.781

added to this reflux solution and stirred for the overall mixture 1 hr at 75℃. The bright yellow solution was filtered and kept refrigerated for crystallization. After a few days, block-sized, yellow-coloured single crystals suitable for SCXRD were obtained. Crystals were isolated by filtration and air-dried. Yield: 0.422 g, (58%), Anal. Calc. for $C_{21}H_{20}N_4O_5PbS_2Zn$: C, 33.85; H, 2.71; N, 7.52. Found: C, 33.82; H, 2.64; N, 7.49%. IR (KBr cm⁻¹) selected bands: ν(C=N), 1620 m, ν(NCS), 2086s, ν(SCN), 2147 m, ν(Ar–O),1357 s, FT-Raman (cm⁻¹) selected bands: ν(C=N), 1632 s, ν(NCS), 2115 s, ν(SCN), 2198 m, ¹H NMR (DMSO-d6, 400 MHz): δ (ppm): 3.61 (s, 3H¹), 6.56–6.97 (m, H²–H⁴), 8.35 (m, 1H⁶), 3.87–4.25 (s, 2H⁷), 3.13–3.61 (s, 6H⁷), UV–Vis λ_{max} (DMSO): 277, and 358 nm.

Scheme 1 Synthetic Strategy for Salen (H_3L) and the Coordination Polymer
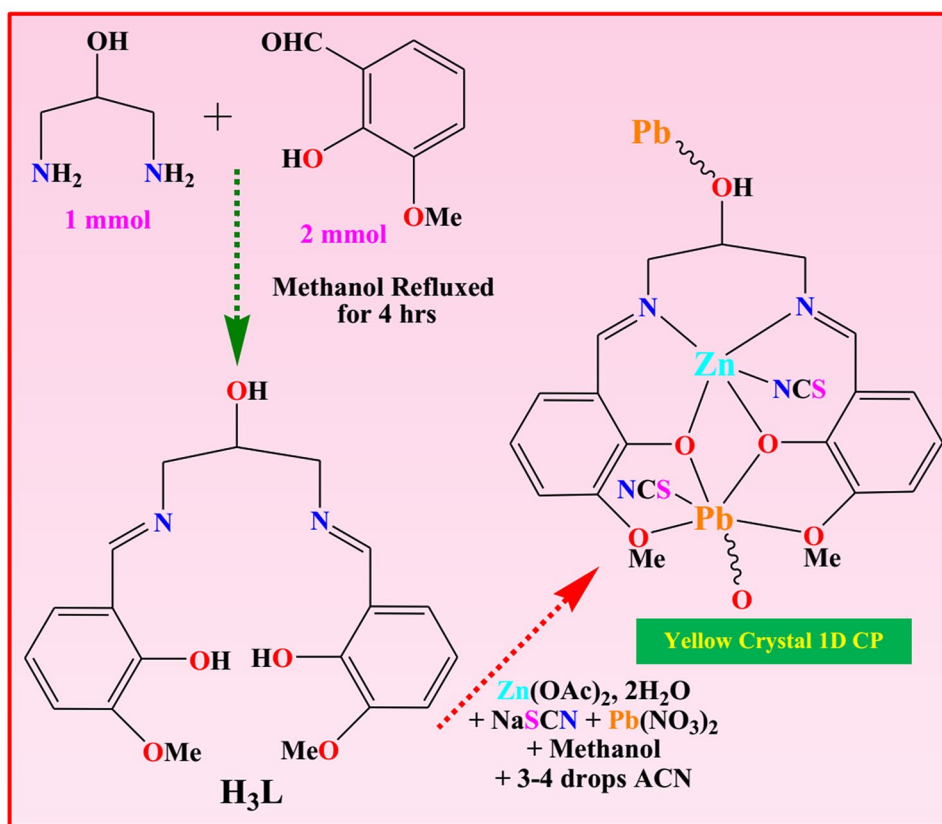
3 Results and Discussion

3.1 Synthetic Rationalization

The ligand was synthesized using the literature method (Scheme 1) [76]. Pb(II)-Salen complex derived from H_3L and thiocyanate spacer were prepared in moderate good yield by selecting the more familiar in situ procedure (Scheme 1). Herein single crystals were not grown in methanol solvent alone; hence, we used a few drops of acetonitrile to promote better diffracting-quality crystals suitable for SCXRD (Scheme 1). The complex is 1D polymer confirmed by SCXRD, being formulated as $[(Zn)(Pb)(L)(\eta^1\text{-NCS})(\eta^1\text{-}SCN)]_n$. H_3L is a unique bicompartmental ligand identical to previously reported Salen [30–32, 77–84]. It discloses basic imitators since it encompasses two imines, two phenols, two alkoxys, and one weakly acidic aliphatic –OH group. Salen ligand always produces an N_2O_2 imine chelating position after deprotonation [85]. Tetradentate N_2O_2 imine chelating site and an additional O_4 compartment trapped by Zn and Pb ions in the presence of thiocyanate spacers (Scheme S2B) together with a flexible –OH arm is Pb(II) ions coordinated. Hence, the aliphatic –OH group played an essential role in participating in supramolecular self-assembly. All the compartmental Salen investigated the synthesis of various heteronuclear complexes [30–32, 77–84]. But H_3L

explored only a few examples of heteronuclear compounds [76]. So far, CPs of weakly acidic aliphatic –OH coordinated Pb(II) ions are rare in the literature. The incredible beauty of the prepared compound and the DFT perspectives justify its novelty.

3.2 Spectroscopic Characterization

The IR and Raman spectroscopy characterized Salen and the CP. The important imine (C=N) stretching vibration of the ligand was identified near 1661 cm^{-1} [86] (Fig. S1). The complex, the stretching vibration bands for IR and Raman (C=N) are moved to 1620 cm^{-1} (Fig.S1) and 1632 cm^{-1} (Fig.S2). The reference spectral data support the coordination of the azomethine nitrogen atom to the zinc metal centre [87]. Thiocyanate spacers (SCN$^-$) displayed two strong bands in 2086, 2147 cm^{-1} (**1**) (IR) and 2115, 2198 cm^{-1} (**1**) (for Raman). Such splitting patterns of the thiocyanate spacer are attributed to two distinct binding modes with the Zn and Pb metal ions [88]. Ar–O stretching frequency near 1239 cm^{-1} is identical with reported Salen-type ligands. The UV–Vis absorption spectra of the Salen and the complex have been analyzed in methanol and DMSO. Ligands exhibit two distinct bands at 341 nm and 425 nm (Fig.S3) for $\pi \rightarrow \pi^*/n \rightarrow \pi^*$

Fig. 1 The ORTEP diagram of the CP (Considering 30% probability)
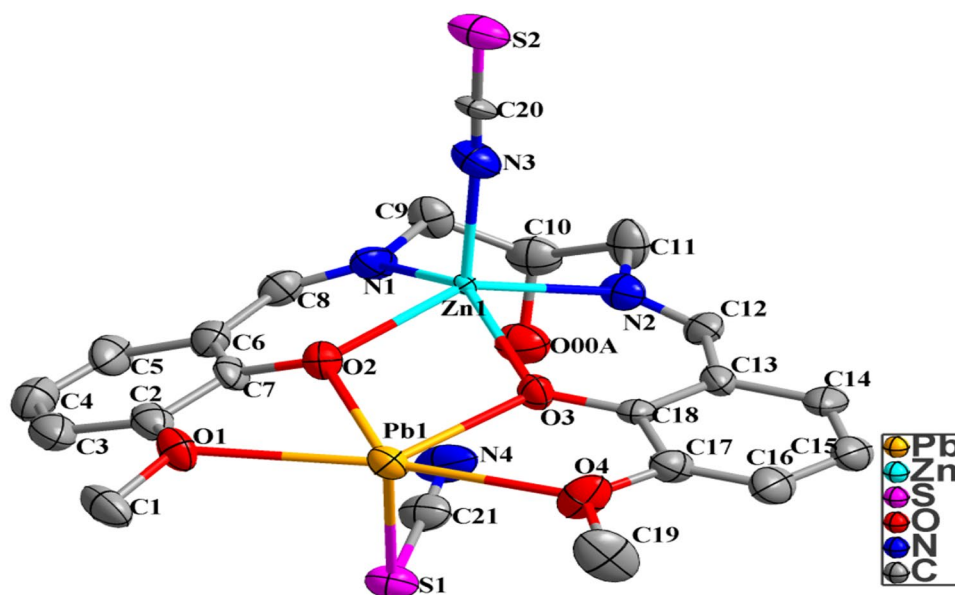
type transitions. In contrast, complex exhibits a strong ligand–based UV domain at 277, 358 nm (Fig.S4) because of the L → M charge-transfer transition ($\pi \to \pi^*/n \to \pi^*$) [87, 89]. The above spectral feature is identical to the previously reported Salen [90, 91]. The UV spectral-domain supports the coordination mode of the Salen ligand with Zn and Pb metal ions. The credit of d^{10} configuration and diamagnetic nature of zinc metal ion, no metal centric d-d broad absorption band has been identified. The NMR spectroscopic tool (^{1}H & ^{13}C NMR) well- characterized the Salen and the CP (Fig.S5-Fig.S6) (Scheme S5). Free Salen in the region δ 5.0–8.0 ppm found no broad peak, suggesting the free -NH$_2$ group absence. The NMR peak value at δ 4.08 ppm identified the aliphatic -OH[8] proton. The phenolic protons (OH[5]) are associated with the defined broad peak at δ 13.91 ppm. The protons (H[6]) attached to the imino carbon are downfield shifted δ 8.65 ppm [90, 91] due to the influence of the combined effect of phenolic –OH and imino N groups in its close vicinity. The peaks within the range δ 7.37–7.38 ppm correspond to the aromatic protons (H[2]–H[4]). The three methyl protons (OCH[1]$_3$) attached to the aromatic oxygen appear at δ 3.83–3.86 ppm. For complex, the coordination mode of azomethine nitrogen was assigned to the downfield shift of the azomethine proton signal from the ligand. The OH proton (OH[5]) signal at the ligand disappeared in the ^{1}H NMR spectra of the complex, showing deprotonation and coordination of the oxygen with zinc metal ion [90, 91] (Fig.S7). ^{13}C NMR spectra of the ligand showed the azomethine (CH=N) carbons at 168.40–172.62 ppm (Fig. S6). The other significant ^{13}C NMR peaks for Salen were observed at 55.19–67.69 (O-CH$_3$),106.12–132.93 (Arom-C), 152.26 (C–OH) ppm.

3.3 SEM and PXRD

Scanning electron microscope (SEM) images characterized the size and morphological structure of the as-prepared complex. The SEM micrograph (Fig.S8) directly supports the morphology of the complex plate shape. Furthermore, the PXRD method studied the as-prepared compound phase purity and crystallinity and recorded diffraction patterns at room temperature. At room temperature, the complex recorded PXRD designs within the range ($2\theta = 40^0$–50^0) at a wavelength (λ) of 1.54 Å. Because of their crystalline existence, Fig.S9 displayed well-defined single sharp PXRD peaks. PXRD observed patterns of the complex's bulk materials are like the patterns simulated from SCXRD CIF data. Therefore, the single crystals and the bulk material are the same. The PXRD analytical results will confirm the phase purity of each bulk sample.

4 X-Ray Crystal Structure Description

4.1 Crystal Structure of Complex

Single crystal diffraction study of good quality block shape crystal reveals the complex crystallizes in the monoclinic space group (P21/c, Z=4). The asymmetric unit is electronically neutral. It contains one deprotonated ligand (L^{2-}) form and full occupancy of crystallographically independent Zn^{2+} and Pb^{2+} metal ions. Additionally, it also has two

Thiocyanate ions with formula $[(Zn)(Pb)(L)(\eta^1\text{-NCS})(\eta^1\text{-SCN})]_n$ (**1**) (Fig.S1). The asymmetric units charge (cationic charge 4) is balanced by the two anionic charges from the one deprotonated ligand (L^{2-}) and two more anionic charges from the two Thiocyanate ions. The heteronuclear complex ORTEP diagram is shown in Fig. 1. The preferred bond distance and bond angles are given in the supporting information (Table S1).

The ligand design visualizes the presence of two multidentate pockets, which can accommodate the metal ions towards the formation of bimetallic clustered. The pockets are pocket 1 (pentadentate pockets comprised of 3O and 2 N) and pocket 2 (tetradentate comprised of 4O) (Fig. 2a). Interestingly, out of three hydroxyl groups, the two hydroxyl groups are deprotonated, and the third one (-O00AH) remains un-dissociated. In addition, the two hydroxyl groups (-O3H and –O2H), which are located towards each other on the H_3L, are deprotonated during the reaction and hold the metal ions viz Zn^{2+} (the inner core of L^{2-}) and Pb^{2+} (the outer core of L^{2-}) through η^2 mode. The two Thiocyanate spacers are attached to each metal ion in the opposite direction. Therefore, resulting in a bi-nuclear heterometallic

Fig. 2 **a** Schematic presentation for the presence of two pockets in H_3L, and **b** formation of bi-nuclear heterometallic cluster
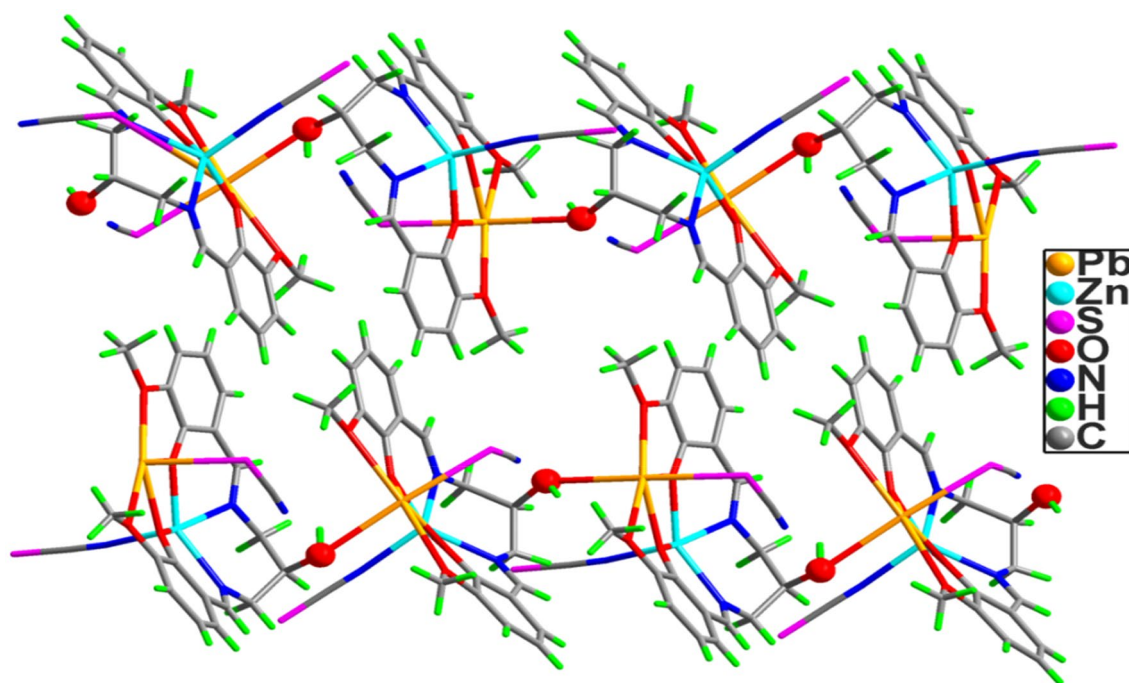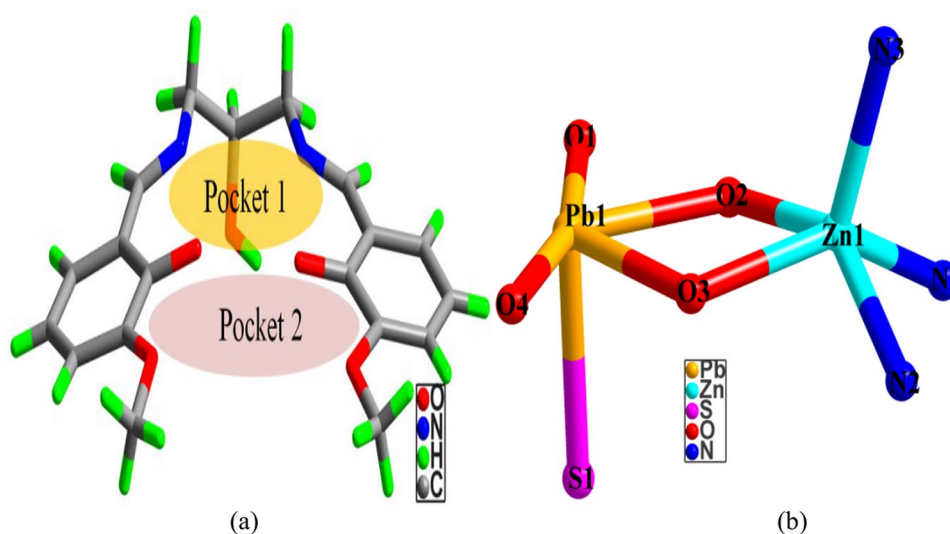
(a)　　　　　　　　　　　　(b)

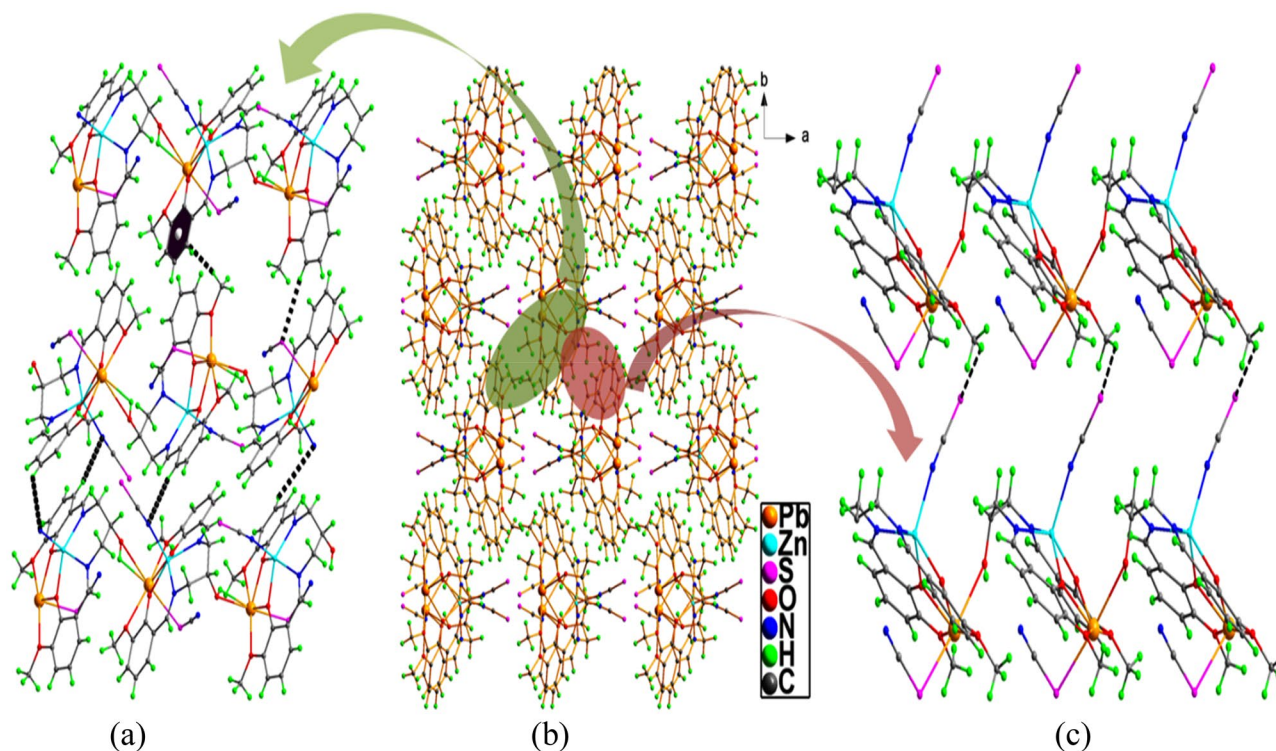**Fig. 3** The perspective view of the polymeric network of the CP

Fig. 4 The non-covalent interaction within complex leading to the formation of 3D polymeric network: **a** representation of C-H⋯π and hydrogen bonding, **b** 3D view of the complex and **c** S⋯H interaction

Table 2 Symmetry operated possible interaction parameters

Interaction components	Bond distance (Å)	Bond angle (°)
C19–H19C⋯⋯Cg(C2–C7)″ (″=2 − x, 1 − y, 1 − z)	3.01(2)	171.67(2)
C4–H4⋯⋯N3# (#=x, − 1+y, z)	3.14(2)	113.77(2)
C1–H1C⋯⋯S2″ (″=− 1+x, 0.5 − y, 0.5+z)	2.97(6)	129.81(2)
C16–H16⋯⋯S1# (#=x, − 1+y, z)	3.09(6)	167.87(2)
C15–H15⋯⋯N3# (#=x, − 1+y, z)	2.93(2)	132.97(1)
C5 − H5⋯⋯N3″ (″=1 − x, − y, 1 − z)	2.76(2)	148.19(1)

cluster (Fig. 2b). Interestingly, in this modus operandi of Thiocyanate, the Pearson theory holds very well [92]. Between Zn^{2+} and Pb^{2+} ion, the former is a hard acid, and the latter is a soft acid. Thus, the sulfur atom (soft base) of Thiocyanate is preferably linked to the soft acid (Pb^{2+}), and the nitrogen atom (hard base) is connected to the hard acid (Zn^{2+}) (Fig. 1 and Fig. 3b). Furthermore, Cambridge Structural Database studies (Histogram plots, Fig.S11) supported the Thiocyanate N-bonded preferred binding with d^{10} metal ions (Zn/Cd) [25]. Zn(II) occupies inner N_2O_2, and Pb(II) occupies the outer O_4 compartments. One of the striving stereochemical features is the competitive occupancy of Zn(II) vs. Pb(II) metal ions. The radius factor between Zn(II) and Pb(II) solves the stereochemical occupancy. The significant Pb(II) ionic radius (133 pm) is greater than that of Zn(II)

metal ions. Therefore, it is difficult for Pb(II) to be accommodated in the inner N_2O_2 compartment, where minor small size Zn(II) fits well at the outer O_4 cavities. Hence Pb(II) ion provides well in the open external O_4 pit [93]. The Zn-Pb bond distances [3.726–3.540 Å] are comparable with the literature-reported Pb(II)-heteronuclear complexes [30–32, 77–84]. The values of the Pb-N, Pb–O, and Pb–S (SCN) bond distances rejected the concept of the Tetrel bonding concept, one of the popular bonding features for the Pb(II) complexes described in the literature (Tables S2, S3).

The complex X-ray crystal structure reveals the formation of the 1D polymeric network by the construction of a bridge between the un-dissociated hydroxyl group (-O00AH) of one asymmetric unit with the metal center (Pb^{2+}) of another asymmetric unit (Fig. 3). The un-dissociated hydroxyl

(-O00AH) group binds with lead ion over zinc due to the vacant coordination space left on lead (vide infra) than the zinc. Though the zinc can have the ability to form six coordination complex the attachment of un-dissociated hydroxyl (-O00AH) group to zinc metal ion in the opposite direction of thiocyanate on zinc presumably bring the two asymmetric units close enough to occur severe steric crowding between the methyl groups on each asymmetric unit and the resulted polymeric system becomes highly unstable. Interestingly, this 1D polymeric network undergoes several non-covalent interactions (S···H [94] (Fig. 4c), C–H···π and hydrogen bonding (Fig. 4a), Table 2) to form a 3D network (Fig. 4b).

The binding fashion of both ligand and Thiocyanate ions is presented in Figure S12. The ligand H_3L is symmetrically bound to the two Pb and one Zn metal ions through η^1-oxygen, η^2-oxygen, and η^1-nitrogen, and two thiocyanate ions are separately linked to lead and zinc via same binding fashion, μ_1-η^1. This coordination action provided the zinc metal ion has perfect square bipyramidal geometry (Fig. 5a) constructed from 3 N and 2O atoms. The Addison structural parameter (τ) [95] value helps to determine the correct stereochemical environment around the Zn metal ions, ($\tau = (\beta - \alpha)/60^0$ where β and α are the two largest angles around the central atom: $\tau = 0$ for perfect square pyramidal and 1 for an ideal trigonal geometry). Zinc metal ions are five coordinated perfect square bipyramidal ($\tau = 0.03$), fulfilled by binding action from 2O and 3 N (Fig. 5a). Amusingly, though the lead ion is six coordinated, it shows a classical Hemi-directed coordination sphere (Fig. 5b). In this complex, lead is in + 2 oxidation state and one of the

post-transition elements with total electronic configuration $[Xe]4f^{14}5d^{10} 6s^2$ and displayed inert-pair effect. The $6s^2$ electron is inert to participate in the oxidation state process/ covalent bond formation. It behaves as a lone pair which causes the non-spherical charge allocation around the lead ion, i.e., the distribution of ligands around the lead leaves some vacant space (identifiable void). Thus, this complex's lead (II) ion preferred Hemi-directed coordination over Holo-directed coordination sphere [46, 55–57].

4.2 CP Novel X-Ray Crystal Structure: Comparison with Analogous Complexes

The crucial information of the coordination chemistry involving flexible weakly acidic aliphatic –OH group appending compartmental Salen (H_3L) is limited in the literature [76]. Therefore, a few examples of complexes [Cu(HL)Na(NO$_3$)(MeOH)], [Cu(HL)Hg(Cl)$_2$], [Cu(HL)Zn(NO$_3$)(H$_2$O)]NO$_3$, [Cu(HL)(H$_2$O)Sm(NO$_3$)$_3$], [Cu(HL)(H$_2$O)Bi(NO$_3$)$_3$], [Cu(HL)Pb(NO$_3$)$_2$], and [Cu(HL)Cd(NO$_3$)$_2$] respectively, are explored with H_3L, particularly in the absence of thiocyanate spacer [76]. We envisioned introducing a flexible aliphatic hydroxyl group into such Salen to check the enhancement of the H-bonding capability of the afforded CP, or it may be coordinated with metal ions like Pb(II). Thereby, control the crystal structural features and dimensionality in the resulted solids. Our target might be if the –OH group remained uncoordinated with the metal ions or involved in H-bonding. Thereby generates supramolecular architecture expanding from discrete to 3D network. Published heteronuclear complexes were limited
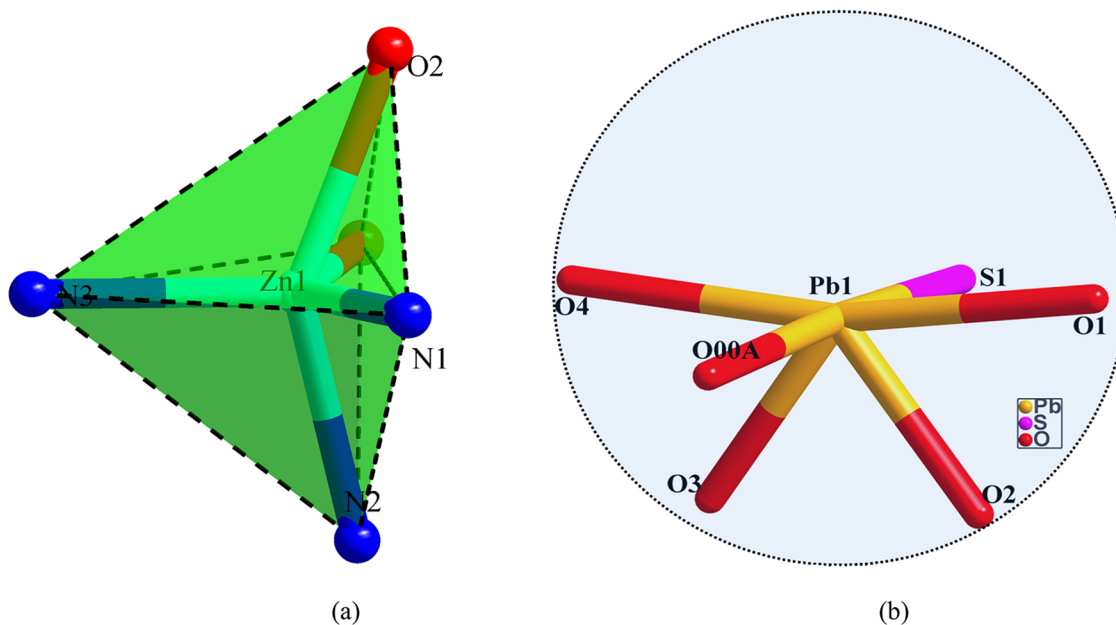

(a)

(b)

Fig. 5 **a** Five coordinated perfect square bipyramidal geometries around zinc and **b** hemi-directed coordination sphere around lead

in the literature [76] using the identical Salen. We observed most of the complexes without using thiocyanate spacers. Concerning our complex, it is 1D hetero-binuclear CP fabricated in the spirit of NaSCN. Meanwhile, X-ray crystal structure envisages that in our CP, heavier Pb(II) ions are coordinated with the weakly acidic –OH group of the ligand, which establishes its novelty. The –OH group appending activity leads to 1D CP formation. Furthermore, all previously published heteronuclear complexes internal and external compartments occupancy usual, but our prepared CP two distinct compartment occupancy highlighted. Five coordinated trigonal bipyramid geometries around zinc metal ion and Hemi-directed coordination sphere around the lead. Another remarkable feature of the reported complexes explores that the ligand can accommodate quite comfortably all the additional metal ions at an open O_4 compartment, irrespective of the size and charge of the ions, demonstrating the flexible nature of the ligand [76]. The radius factor governs the 2nd Pb metal ions accommodation at the external O_4 compartment in our complexing system. The reported complexes show only usual non-covalent interactions, e.g., H-bonding, π–π, and C–H–π stacking, responsible for understanding possible supramolecular topologies. Interestingly, our 1D polymeric network undergoes several non-covalent interactions (S···H, C–H···π and hydrogen bonding to form a 3D grid. However, a significant difference was observed for the overall composition of the previously reported complexes, non-appending –OH group leads mononuclear or discrete regarding the present CP. Remarkably, previous reports [76] show that in most cases, they are cocrystals, primarily when o-ethoxy salicylaldehyde is used instead of ortho vanillin. The co-crystallization process is described as the tendency of the water molecule to be encapsulated into the O_4 compartment. Therefore, the stabilization of two-component and even three-component cocrystals [76]. The role of the steric influence of o-ethoxy over o-methoxy potentially considered such co-crystallization processes [76]. In contrast to the other structural findings literature, the most exciting observation of the previously reported complexes is the helical twisting in the coordinated Salen as manifested by the torsion angles of N_2O_2 and O_4 compartments being estimated to be − 31.86º and − 29.82º, respectively [76]. Contrary, such helical twisting is absent in our synthesized CP. Finally, the above discussion investigates that our prepared CP possesses a new crystal structure associated with 1D polymer and –OH groups with pendent supramolecular topologies.

5 Supramolecular Topologies: Hirshfeld Surface

The flexible aliphatic –OH group's role is directed for self-organization in the crystal structure. The supramolecular topologies are theoretically correlated with the Hirshfeld Surface mapping. The hydrogen bonds were considered to understand the possible supramolecular topologies. HS calculations are performed to examine the intermolecular interactions of molecular crystals of the metal complex. These calculations and 2D fingerprint [96] plots representations of the metal complex are obtained using the CrystalExplorer17.5 program [97]. The calculations were considered using the metal complex with the *.cif extension file. It is based on the electron distribution calculated as the sum of the spherical atomic electron densities [98, 99]. The normalized contact distance of molecules, d_{norm}, and the distance from a point on the surface to the nearest nucleus outside the surface indicate. It allows the identification of regions that are particularly important for di-molecular interactions. It is also a visual representation of the distance from a point on the surface to the nearest nucleus. Intermolecular contacts in the crystal lattice, that is, two-dimensional fingerprint graphic representations, are visual representations of the combination of numerical values of de and di (Fig. 6) [100]. The normalized contact distance $d_{norm} = d_i − r_i^{vdw}/r_i^{vdw} + d_e − r_e^{vdw}/r_e^{vdw}$[100], where r_i^{vdw} and r_e^{vdw} are the van der Walls radii of the atoms. If the dnorm is negative, the intermolecular contact is expected to be shorter than rvdw, on the other hand, if the d_{norm} is positive, it is expected to be longer. The red-white-blue colors in the HS map indicate the shortest intermolecular contact. The contact around the rvdw separation and the longer intermolecular contact distance, respectively (Fig. 6). Figure 7 shows contributions to HS for the complex, % of H···H, N···H, H···S, C···H, and H···C interactions. During the formation of the molecular packaging, the HS approach confirms the hydrogen interaction because the hydrogen atom interactions of the CP are more significant than the others. It seems that there are many interactions, such as H/H, C/H/H/C, and N/H/H/N. Hydrogen bonds and van der Waals interactions seem to be more common in molecular packaging than in other types of interaction [96, 101].

6 FMO Approach

Using DFT, it is possible to comment on the chemical and biological activities of the molecules. The quantum chemical parameters provide information about many chemical properties of the metal complex. Among the calculated quantum chemical parameters of metal complex, two parameters that help interpret the activity are HOMO (highest occupied molecular orbital) and LUMO (lowest unoccupied molecular orbital). The HOMO parameter indicates the electron-donating ability of the metal complex. The chemical activity of the molecule with the highest numerical value of this parameter is the highest [102]. The LUMO parameter indicates the electron acceptability of the metal complex. The
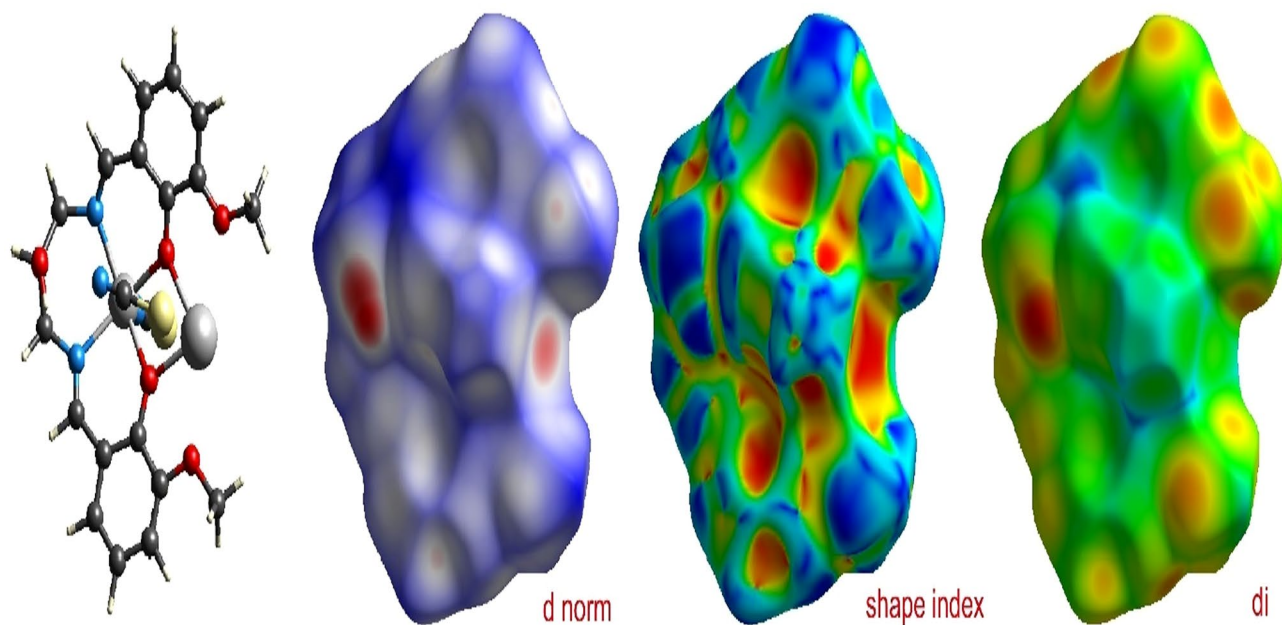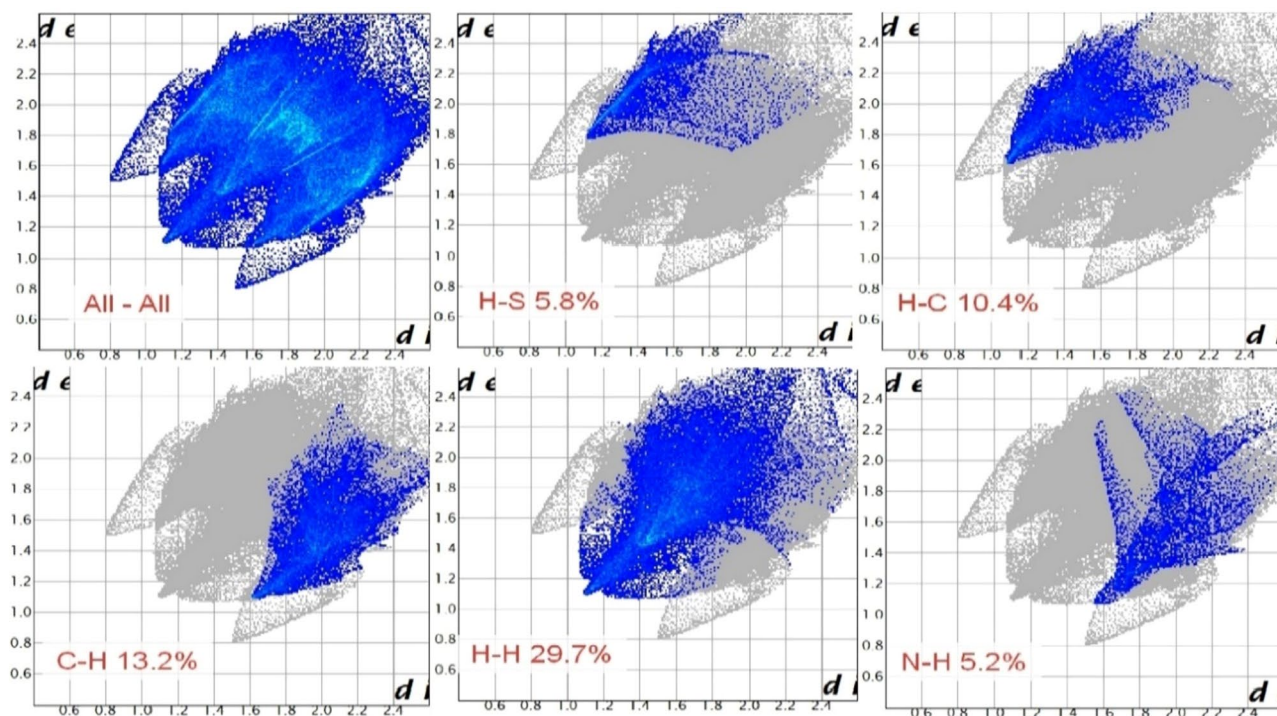
Fig. 6 HS mapped of the complex with d_{norm} and d_i

Fig. 7 2D fingerprint plot of the complex showing all interactions, delineated into % of H···H, N···H, H···S, C···H, and H···C type interactions

activity of the molecule with the lowest numerical value of this parameter is higher. Again $\Delta E(E_{HOMO}\text{-}E_{LUMO})$, which can be used to compare the chemical activity of molecules. The molecule with the smallest numerical value of these parameters is considered to have the highest activity [103]. The numerical value of the electronegativity parameter indicates the strength of the atoms in the molecule to attract bond electrons [103]. The increasing electronegativity value of the complex reflects the probability of donating electrons decreases. Further, the parameter is chemical hardness, which is resistance to electron cloud polarization or deformation of chemical species [102]. Chemical hardness is an essential parameter used to compare the reactivity of molecules in both experimental procedures and theoretical calculations [103]. The Gaussian calculated all parameters are given in Table 3. They have many calculated quantum chemical parameters which exist in visual representations. There are four images in Fig. 8. In the first image, the optimized structure of the molecules is given. In the second and third images, the atoms of the HOMO and LUMO orbitals of the molecules are located. The last picture shows the electrostatic potential (ESP). In this image, the red-colored regions are electron-rich and are the electrophilic reactive center. On the other hand, the blue-colored regions are electron-poor regions and are the nucleophilic reactive center. The different areas are shown in green [103].

7 Molecular Docking

To compare the biological activities of the complex, their actions against cancer proteins, which are biological materials, were examined. Proteins used in these calculations are crystal structure of estrogen receptor protein, ID: 1A52, crystal structure of VEGFR kinase (liver cancer) protein, ID: 3WZE, crystal structure of is an allosteric Eya2 phosphatase inhibitor (lung cancer) protein, ID: 5ZMA, and crystal structure of MLK4 kinase (colon cancer) protein, ID: 4UYA.

When examining their biological activities against these cancer proteins, it is seen that the most crucial factor determining the activity is interaction. As metal complexes and cancer proteins interact with each other, it is seen that the biological activities of metal complexes increase. As the interactions of metal complexes increase, it appears to inhibit cancer proteins [70]. In this way, it has been observed that it prevents the spread and development of cancer cells. These chemical interactions are hydrogen bonds, polar and hydrophobic interactions, π-π, and halogen [104, 105]. E_{Total} energy values of the metal complex are given in Table 4. The interactions of proteins are presented in Fig.S13. It is known that the metal complex with the lowest E total energy values has higher biological activity.

Table 3 The calculated quantum chemical parameters of complex

| Basis set	E_{HOMO}	E_{LUMO}	I	A	ΔE	η	σ	χ	Pi	ω	ϵ	dipole	Energy
1. B3LYP/Lanl2dz LEVEL													
Complex	− 4.9868	− 2.1799	4.9868	2.1799	2.8069	1.4034	0.7125	3.5834	− 3.5834	4.5746	0.2186	8.4676	− 40,716.3717
2. HF/Lanl2dz LEVEL													
Complex	− 7.7822	1.3783	7.7822	− 1.3783	9.1605	4.5803	0.2183	3.2020	− 3.2020	1.1192	0.8935	6.3074	− 40,410.4743
3. M062X/Lanl2dz LEVEL													
Complex	− 6.2671	− 1.2610	6.2671	1.2610	5.0061	2.5031	0.3995	3.7640	− 3.7640	2.8301	0.3533	8.7924	− 40,695.9909
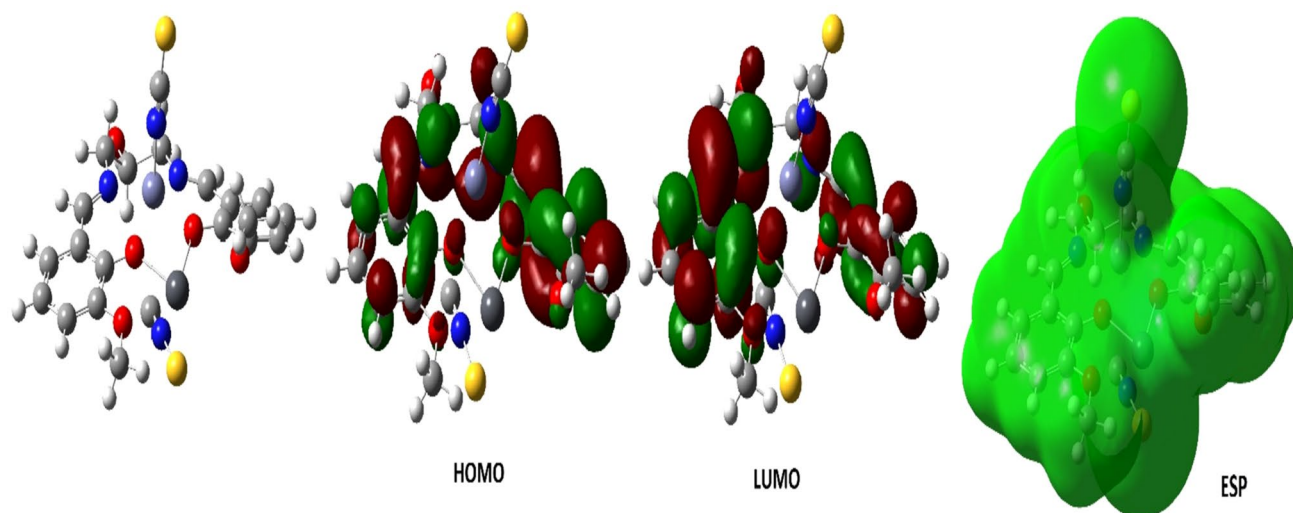
Fig. 8 Representations of the optimized complex structure, HOMO, LUMO, and ESP plot

Table 4 Molecular docking E_{Total} energy

Compounds	Proteins			
Breast cancer	Liver cancer	Lung cancer	Colon cancer
Complex − 290.38	− 305.15	− 295.47	− 276.30

For a molecule to be understood as a good inhibitor candidate for cancer proteins in docking studies, it must have a better activity than FDA (U.S. Food and Drug Administration) approved drug molecules used for working cancer. In this study, 5-Fluorouracil molecule for the commonly used breast cancer protein, Pemigatinib molecule for liver cancer protein, Entrectinib molecule for lung cancer protein, and finally Capecitabine molecule for colon cancer protein were used. As a result of docking calculations, it was seen that the

Fig. 9 Representation of the interaction of the complex with breast cancer (**a**), the interaction with liver cancer (**b**), and the interaction with lung cancer (**c**)
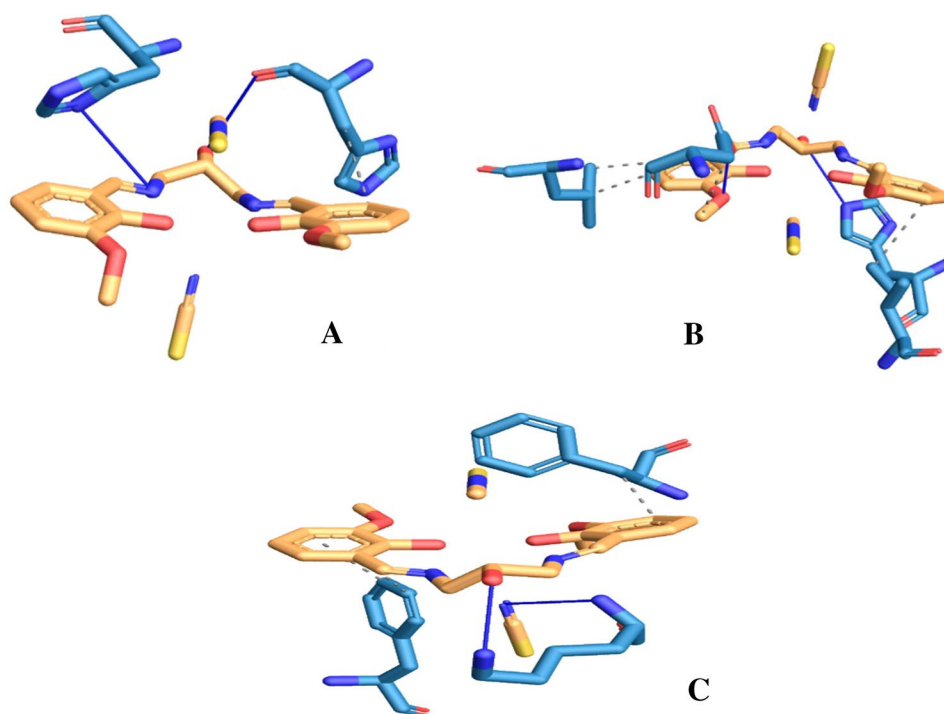
Table 5 Hydrophobic Interactions of protein and the complex

Index	Residue	AA	Distance	Ligand atom	Protein atom
Breast cancer- metal complex					
1	434B	ARG	3.93	4730	3528
2	469A	LEU	3.26	4755	1559
3	472A	LYS	3.29	4753	1589
4	472A	LYS	3.80	4750	1587
5	476A	HIS	3.73	4694	1630
6	480A	ASP	2.89	4746	1676
7	481A	LYS	3.99	4739	1685
8	373B	HIS	3.62	4791	2950
Liver cancer- metal complex					
1	888A	ILE	3.76	3119	742
2	1046A	ASP	3.69	3159	1767
3	1049A	LEU	3.23	3151	1794
4	1049A	LEU	3.81	3149	1796
Lung cancer-metal complex					
1	484B	PHE	3.92	7248	1924
2	484B	PHE	3.83	7242	1923
3	517B	PHE	3.08	7213	2160

In table: *ASP* aspartate, *HIS* histidine, *LEU* leucine, *LYS* lysine, *PHE* phenylalanine

activities of molecules against cancer proteins were higher than the studied metal complex.

7.1 Protein–Ligand Interaction Profiler (PLIP)

After Molecular docking, next is the Protein–Ligand Interaction Profiler analysis [106]. This analysis investigated the chemical interactions between the complex and the proteins and between which proteins they occur. The PLIP observed interactions to be more concentrated in hydrophobic and hydrogen bond types given in Fig. 9 and Tables 5 and 6.

8 Nonlinear Optical Effects (NLO)

Nonlinear optical effects (NLO) are essential parameters for emerging technologies in telecommunications, signal processing, and optical interconnects, providing significant optical modulation, frequency shift, optical logic, optical switching, and optical memory [63]. The dipole moment (μ) is known as polarizability (α) and hyperpolarizability (β). The measure of polarizability (α) and hyperpolarizability (β) is a numerical parameter. That is calculated to predict the nonlinear optical properties of materials. It is calculated using the formulas given below. It is calculated using the formulas given below

$$\mu = \sqrt{(\mu_x^2 + \mu_y^2 + \mu_z^2)} \tag{1}$$

$$\alpha = 2^{-1/2}[(\alpha_{xx} - \alpha_{yy})^2 + (\alpha_{yy} - \alpha_{zz})^2 + (\alpha_{zz} - \alpha_{xx})^2 + 6\alpha_{xx}^2]^{1/2} \tag{2}$$

$$\alpha = \left(\frac{\alpha_{xx} + \alpha_{yy} + \alpha_{zz}}{3}\right) \tag{3}$$

$$\beta_{tot} = [(\beta_{xxx} + \beta_{xyy} + \beta_{xzz})^2 + (\beta_{yyy} + \beta_{yzz} + \beta_{yxx})^2 + (\beta_{zzz} + \beta_{zxx} + \beta_{zyy})^2]^{1/2} \tag{4}$$

The values of polarizability (α_0) and hyperpolarizability (β_{tot}) are calculated in atomic unit (a.u.). Afterward, it is possible to convert these calculated parameters into electrostatic units. ($\alpha : 1 a.u. = 0.148 x 10^{-24} esu$ and $\beta : 1 a.u. = 8.639 x 10^{-33} esu$). In the calculations made on the metal complex, we used HF/lanl2dz basis set. The calculated all parameters are shown in Table 7. The polarizability (α) and hyperpolarizability (β) numerical value suggest that complex exhibits Nonlinear optical effects.

Nonlinear optical effects (NLO) parameters, both Salen and the studied complex numerical value, were calculated.

Table 6 Hydrogen Bonds of protein and the complex

Index	Residue	AA	Distance H-A	Distance D-A	Donor angel	Donor Atom	Acceptor Atom
Breast cancer-metal complex							
1	434B	ARG	1.54	√	√	2.26	124.42
2	434B	ARG	1.49	√	√	2.20	122.75
1	373B	HIS	3.67	X	X	4.00	103.37
2	377B	HIS	3.56	√	√	3.90	102.15
Liver cancer- metal complex							
1	816A	HIS	3.16	X	√	3.71	118.31
2	1046A	ASP	1.76	√	√	2.41	123.80
Lung cancer- metal complex							
1	512B	LYS	2.77	√	X	3.28	110.97
2	512B	LYS	2.27	√	√	3.20	148.58

In table: *ARG* arginine, *ASP* aspartate, *HIS* histidine, *LYS* lysine

Table 7 NLO calculated all parameters for complex

	a.u	esu		a.u	esu
α_{xx}	343.9276	5.09013E−23	β_{xxx}	58.9414	5.092E−31
α_{xy}	− 8.8566	− 1.3108E−24	β_{yyy}	37.7415	3.260E−31
α_{yy}	335.7799	4.96954E−23	β_{zzz}	− 56.5572	− 4.886E−31
α_{xz}	11.9673	1.77116E−24	β_{xyy}	− 329.8068	− 2.849E−30
α_{yz}	24.1934	3.58062E−24	β_{xxy}	− 100.7083	− 8.700E−31
α_{zz}	265.1434	3.92412E−23	β_{xxz}	8.2051	7.088E−32
Δ_{α}	223.6169	3.30953E−23	β_{xzz}	− 91.2813	− 7.886E−31
μ_x	1.0761		β_{yzz}	− 12.5007	- 1.080E−31
μ_y	1.3845		β_{yyz}	117.8870	1.018E−30
μ_z	- 1.7559		β_{total}	376.4049	3.252E−30
μ_g	2.4815				

Table 8 NLO calculated all parameters for Salen ligand

	a.u	esu		a.u	esu
α_{xx}	156.0833	2.31003E-23	β_{xxx}	− 80.6344	− 6.968E−28
α_{xy}	7.8169	1.15691E-24	β_{yyy}	27.9396	2.414E−28
α_{yy}	197.0945	2.917E-23	β_{zzz}	19.6772	1.700E−28
α_{xz}	− 6.5026	− 9.6238E-25	β_{xyy}	113.8998	9.842E−28
α_{yz}	− 19.6309	− 2.9054E-24	β_{xxy}	4.2203	3.647E−29
α_{zz}	178.3340	2.63934E-23	β_{xxz}	− 12.3708	− 1.069E−28
Δ_{α}	120.3316		β_{xzz}	− 42.7265	− 3.692E−28
μ_x	0.0803		β_{yzz}	16.6009	1.434E−28
μ_y	0.0624		β_{yyz}	61.4480	5.310E−28
μ_z	− 0.1301		β_{total}	84.819193	7.329E−28
μ_g	0.165147				

The parameters are given in Tables 7 and 8. The studied metal complex's and Salen ligand numerical NLO parameters (used as a reference) were compared. The complex exhibit better optical effects than the Salen ligand. The heteronuclear Zn-Salen complex's NLO properties are scarce in the literature, yet calculated NLO parameters of our synthesized complex are comparable with the literature reported few Zinc metal complexes [107–110].

9 Conclusions

We have synthesized thiocyanate bridging a 1D hetero-binuclear Zn(II)-Pb(II) coordination polymer from H_3L in the presence of NaSCN. The CP is structurally characterized by the Elemental, NMR, SEM, PXRD, and SCXRD studies. SCXRD divulges Zn(II) and Pb(II) metal ions, fulfilling perfect square bipyramidal and Hemi-directed coordination spheres. The exciting consequence of the complex crystal structure explores an unusual helical twist for the coordinated aliphatic –OH group with the lead metal ions. We carried out compelling computational studies of the CP to delineate FMO, the Global chemical parameters, and MEP. Hirshfeld Surface explained the non-covalent supramolecular interactions, particularly hydrogen bonds that arise due to the ligand's flexible aliphatic –OH pendant. The H/H, C/H/H/C, and N/H/H/N further controlled the supramolecular network. Van der Waals interactions appear to be essential for the molecular packaging of the crystal structure. PLIP and MD, like advanced experiments, have successfully discovered new biological activities. The parameter calculated by the NLO enhances the non-linear optical effect of the CP over the Salen ligand. Our workshop will continue to examine the formation of heteronuclear CPs or the ability to form innovative co-crystallized compounds with biological effectiveness.

Declarations

References

1. M. Zhao, J. Su, J. Zhang, J.Y. Wu, Y.P. Tian, Acta Crystallogr. C **71**, 799–803 (2015)
2. D. Zhao, D.J. Timmons, D. Yuan, H.C. Zhou, Acc. Chem. Res. **44**, 123–133 (2011)
3. L.R. Mingabudinova, V.V. Vinogradov, V.A. Milichko, E. Hey-Hawkins, A.V. Vinogradov, Chem. Soc. Rev. **45**, 5408–5431 (2016)
4. O.R. Evans, W. Lin, Acc. Chem. Res. **35**, 511–522 (2002)
5. J.A. Sheikh, A. Clearfield, Inorg. Chem. **55**, 8254–8256 (2016)
6. J.M. Frost, K.L.M. Harriman, M. Murugesu, Chem. Sci. **7**, 2470–2491 (2016)
7. Z.G. Gu, C.H. Zhan, J. Zhang, X.H. Bu, Chem. Soc. Rev. **45**, 3122–3144 (2016)
8. S.S. Zhao, J. Yang, Y.Y. Liu, J.F. Ma, Inorg. Chem. **55**, 2261–2273 (2016)
9. A. Douvali, A.C. Tsipis, S.V. Eliseeva, S. Petoud, G.S. Papaefstathiou, C.D. Malliakas, I. Papadas, G.S. Armatas, I. Margiolaki, M.G. Kanatzidis, T. Lazarides, M.J. Manos, Angew. Chem. Int. Ed. **54**, 1651–1656 (2015)
10. C.J. Doonan, C.J. Sumby, CrystEngComm **19**, 4044–4048 (2017)
11. I. Nath, J. Chakraborty, F. Verpoort, Chem. Soc. Rev. **45**, 4127–4170 (2016)
12. R.R. Salunkhe, C. Young, J. Tang, T. Takei, Y. Ide, N. Kobayashi, Y. Yamauchi, Chem. Commun. **52**, 4764–4767 (2016)
13. J. Tang, Y. Yamauchi, Nat. Chem. **8**, 638–639 (2016)
14. W. Zhang, X. Jiang, Y. Zhao, A. Carné-Sánchez, V. Malgras, J. Kim, J.H. Kim, S. Wang, J. Liu, J.S. Jiang, Y. Yamauchi, M. Hu, Chem. Sci. **8**, 3538–3546 (2017)
15. R.R. Salunkhe, Y.V. Kaneti, Y. Yamauchi, ACS Nano **11**, 5293–5308 (2017)
16. R. Robson, in *Comprehensive Supramolecular Chemistry*, vol. 6, ed. by J.L. Atwood, J.E.D. Davies, D.D. MacNicol, F. Vogtle, R.B. Toda (Pergamon, Oxford, 1996), p. 733
17. J.-P. Sauvage, *Transition Metals in Supramolecular Chemistry, Perspectives in Supramolecular Chemistry*, 5th edn. (Wiley, London, 1999)
18. D. Braga, F. Grepioni, A.G. Orpen, *Crystal Engineering: From Molecules and Crystals to Materials* (Kluwer Academic, Dordrecht, The Netherlands, 1999)
19. F. Nouar, J.F. Eubank, T. Bousquet, L. Wojtas, M.J. Zaworotko, M. Eddaoudi, J. Am. Chem. Soc. **130**, 1833 (2008)
20. F.G. Vogt, J.S. Clawson, M. Strohmeier, A.J. Edwards, T.N. Pham, S.A. Watson, Cryst. Growth Des. **9**, 921 (2009)
21. S. Shimomura, M. Higuchi, R. Matsuda, K. Yoneda, Y. Hijikata, Y. Kubota, Y. Mita, J. Kim, M. Takata, S. Kitagawa, Nat. Chem. **2**, 633 (2010)
22. M. Andruh, D.G. Branzea, R. Gheorghe, A.M. Madalan, CrystEngComm **11**, 2571–2584 (2009)
23. M. Chen, H. Zhao, C.S. Liu, X. Wang, H.Z. Shi, M. Du, Chem. Commun. **51**, 6014–6017 (2015)
24. C.E. Housecroft, Dalton Trans. **43**, 6594–6604 (2014)
25. A. Hazari, L.K. Das, A. Bauza, A. Frontera, A. Ghosh, Dalton Trans. **43**, 8007–8015 (2014)
26. D.J. Majumdar, S. Dey, A. Kumari, T.K. Pal, K. Bankura, D. Mishra, Spectrochim. Acta. A **254**, 119612 (2021)
27. D.J. Majumdar, D. Das, S.S. Sreejith, S. Nag, S. Dey, S. Mondal, K. Bankura, D. Mishra, Inorg. Chim. Acta. **496**, 119069 (2019)
28. A. Jana, S. Majumder, L. Carrella, M. Nayak, T. Weyhermueller, S. Dutta, D. Schollmeyer, E. Rentschler, R. Koner, S. Mohanta, Inorg. Chem. **49**, 9012 (2010)
29. M. Nayak, R. Koner, H. Stoeckli-Evans, S. Mohanta, Cryst. Growth Des. **5**, 1907 (2005)
30. S. Roy, M.G.B. Drew, A. Bauzá, A. Frontera, S. Chattopadhyay, Dalton Trans. **46**, 5384–5397 (2017)
31. S. Roy, A. Bhattacharyya, S. Purkait, A. Bauzá, A. Frontera, S. Chattopadhyay, Dalton Trans. **45**, 15048–15059 (2016)
32. A. Bhattacharyya, S. Roy, J. Chakraborty, S. Chattopadhyay, Polyhedron **112**, 109–117 (2016)
33. P. Bhowmik, S. Jana, P.P. Jana, K. Harms, S. Chattopadhyay, Inorg. Chim. Acta. **390**, 53–60 (2012)
34. P. Bhowmik, S. Jana, P.P. Jana, K. Harms, S. Chattopadhyay, Inorg. Chem. Commun. **18**, 50–56 (2012)
35. V. Vieru, T.D. Pasatoiu, L. Ungur, E. Suturina, A.M. Madalan, C. Duhayon, J.-P. Sutter, M. Andruh, L.F. Chibotaru, Inorg. Chem. **55**, 12158 (2016)
36. M.-J. Liu, K.-Q. Hu, C.-M. Liu, A.-L. Cui, H.-Z. Kou, New J. Chem. **40**, 8643 (2016)
37. J. A. Thomas, in: J.L. Atwood, J.W. Steed (Eds.), Encyclopedia of Supramolecular Chemistry, CRC Press, Boca Raton, FL, pp. 1248 (2004)
38. Y. Sui, D.-P. Li, X.-H. Zhou, T. Wu, X.-Z. You, Inorg. Chem. **49**, 1286 (2010)
39. S. Hazra, R. Koner, M. Nayak, H.A. Sparkes, J.A.K. Howard, S. Mohanta, Cryst. Growth Des. **9**, 3603 (2009)
40. S. Sasmal, S. Majumder, S. Hazra, H.A. Sparkes, J.A.K. Howard, S. Mohanta, CrystEngComm **12**, 4131 (2010)
41. S. Bhattacharya, S. Mondal, S. Sasmal, H.A. Sparkes, J.A.K. Howard, M. Nayak, S. Mohanta, CrystEngComm **13**, 1029 (2011)
42. D.L. Reger, T.D. Wright, C.A. Little, J.J.S. Lamba, M.D. Smith, Inorg. Chem. **40**, 3810–3814 (2001)
43. H. Fleischer, D. Schollmeyer, Inorg. Chem. **43**, 5529–5536 (2004)
44. A. Morsali, A.R. Mahjoub, Helv. Chim. Acta. **87**, 2717–2722 (2004)
45. A. Olvera, G. Shi, H. Djieutedjeu, A. Page, C. Uher, E. Kioupakis, P.F.P. Poudeu, Inorg. Chem. **54**, 746–755 (2015)
46. R.J. Gillespie, R.S. Nyholm, Q. Rev. Chem. Soc. **11**, 339–380 (1957)
47. C.A. Randall, A.S. Bhalla, T.R. Shrout, L.E. Cross, J. Mater. Res. **5**, 829–834 (1990)
48. F. Cheng, J. Liang, Z. Tao, J. Chen, Adv. Mater. **23**, 1695–1715 (2011)
49. L. Zhang, Y.-Y. Qin, Z.-J. Li, Q.-P. Lin, J.-K. Cheng, J. Zhang, Y.-G. Yao, Inorg. Chem. **47**, 8286–8293 (2008)
50. G. Mahmoudi, A. Bauzá, A. Frontera, Dalton Trans. **45**, 4965–4969 (2016)
51. M.S. Gargari, V. Stilinović, A. Bauzá, A. Frontera, P. McArdle, D.V. Derveer, S.W. Ng, G. Mahmoudi, Chem. Eur. J. **21**, 17951–17958 (2015)
52. K.S. Pitzer, Relativistic effects on chemical properties. Acc. Chem. Res. **12**, 271–276 (1979)
53. P. Pyykkö, J. P. Desclaux, Relativity and the periodic system of elements. Acc. Chem. Res. **12,** 276−281 (1979)
54. P. Pyykkö, Relativistic effects in structural chemistry. Chem. Rev. **88**, 563−594 (1988)
55. J. R. Thompson, D. Snider, J. E. C. Wren, S. Kroeker, V. E. Williams, D. B. Lenzoff, Eur. J. Inorg. Chem. 88–98 (2017)

56. R.L. Davidovich, V. Stavila, D.V. Marinin, E.I. Voit, K.H. Whitmire, Coord. Chem. Rev. **253**, 1316–1352 (2009)

57. D.L. Reger, M.F. Huff, A.L. Rheingold, B.S. Haggert, J. Am. Chem. Soc. **114**, 579–584 (1992)

58. L.E. Orgel, Spectra of transition-metal complexes. J. Chem. Phys. **23**, 1004–1014 (1955)

59. M.B. Gürdere, Y. Budak, U.M. Kocyigit, P. Taslimi, B. Tüzün, M. Ceylan, In Silico Pharmacol. **9**(1), 1–11 (2021)

60. M.T. Riaz, M. Yaqub, Z. Shafiq, A. Ashraf, M. Khalid, P. Taslimi, I. Gulçin, Bioorg. Chem. **114**, 105069 (2021)

61. Y. Sheena Mary, Y. Shyma Mary, S. Armaković, S. J. Armaković, B. Narayana, J. Biomol. Struct. Dyn. 1–11 (2020)

62. Y.S. Mary, C.Y. Panicker, M. Sapnakumari, B. Narayana, B.K. Sarojini, A.A. Al-Saadi, C. Van Alsenoy, J.A. War, H.K. Fun, Spectrochim. Acta. A **138**, 529–538 (2015)

63. P.G. Lacroix, S. Di Bella, I. Ledoux, Chem. Mater. **8**(2), 541–554 (1996)

64. D.J. Majumdar, B. Tüzün, T.K. Pal, R.V. Saini, K. Bankura, D. Mishra, Polyhedron **210**, 115504 (2021)

65. M. J. Frisch, G. W. Trucks, H. B. Schlegel, G. E. Scuseria, M. A. Robb, J. R. Cheeseman, G. Scalmani, V. Barone, G. A. Petersson, H. Nakatsuji, X. Li, M. Caricato, A. V. Marenich, J. Bloino, B. G. Janesko, R. Gomperts, B. Mennucci, H. P. Hratchian, J. V. Ortiz, A. F. Izmaylov, J. L. Sonnenberg, D. Williams-Young, F. Ding, F. Lipparini, F. Egidi, J. Goings, B. Peng, A. Petrone, T. Henderson, D. Ranasinghe, V. G. Zakrzewski, J. Gao, N. Rega, G. Zheng, W. Liang, M. Hada, M. Ehara, K. Toyota, R. Fukuda, J. Hasegawa, M. Ishida, T. Nakajima, Y. Honda, O. Kitao, H. Nakai, T. Vreven, K. Throssell, J. A. Montgomery, Jr., J. E. Peralta, F. Ogliaro, M. J. Bearpark, J. J. Heyd, E. N. Brothers, K. N. Kudin, V. N. Staroverov, T. A. Keith, R. Kobayashi, J. Normand, K. Raghavachari, A. P. Rendell, J. C. Burant, S. S. Iyengar, J. Tomasi, M. Cossi, J. M. Millam, M. Klene, C. Adamo, R. Cammi, J. W. Ochterski, R. L. Martin, K. Morokuma, O. Farkas, J. B. Foresman, J. V. Ortiz, J. Cioslowski, D. J. Fox, Gaussian 09, revision D.01. Gaussian Inc, Wallingford CT, (2009)

66. L.K. Ojha, B. Tüzün, J. Bhawsar, J. Bio Tribo Corros. **6**(2), 1–10 (2020)

67. B. Tüzün, E. Saripinar, J. Iran. Chem. Soc. **17**(5), 985–1000 (2020)

68. D.W. Ritchie, V. Venkatraman, Bioinformatics **26**(19), 2398–2405 (2010)

69. A. T. Bilgiçli, H. G. Bilgicli, C. Hepokur, B. Tüzün, A. Günsel, M. Zengin, M. N. Yarasir, Appl. Organomet. Chem. e6242 (2021)

70. U. M. Koçyiğit, P. Taslimi, B. Tüzün, H. Yakan, H. Muğlu, E. Güzel, E. (2020). J. Biomol. Struct. Dyn. 1–11 (2020)

71. G. M. Sheldrick, SADABS, a software for empirical absorption correction, Ver.2.05. University of Göttingen, Göttingen (2002)

72. SMART & SAINT Software Reference manuals Version 6.45. Bruker Analytical X-ray Systems, Inc., Madison (2003)

73. SHELXTL Reference Manual Ver. 6.1. Bruker Analytical X-ray Systems, Inc., Madison (2000)

74. G. M. Sheldrick, SHELXTL, a software for empirical absorption correction Ver.6.12. Bruker AXS Inc., Madison (2001)

75. O.V. Dolomanov, L.J. Bourhis, R.J. Gildea, J.A.K. Howard, H. Puschmann, OLEX2, *OLEX2*: a complete structure solution, refinement, and analysis program. J. Appl. Crystallog. **42**, 339–341 (2009)

76. M. Dolai, T. Mistri, A. Panja, M. Ali, Inorg. Chim. Acta. **399**, 95–104 (2013)

77. P.K. Bhaumik, A. Banerjee, T. Dutta, S. Chatterjee, A. Frontera, S. Chattopadhyay, CrystEngComm **22**, 2970–2977 (2020)

78. A. Hazari, L.K. Das, A. Bauzá, A. Frontera, A. Ghosh, Dalton Trans. **45**, 5730–5740 (2016)

79. S. Roy, A. Dey, M.G.B. Drew, P.P. Ray, S. Chattopadhyay, New J. Chem. **43**, 5020–5031 (2019)

80. S. Dey, S. Sil, B. Dutta, K. Naskar, S. Maity, P.P. Ray, C. Sinha, ACS Omega **22**(4), 19959–19968 (2019)

81. S. Mirdya, S. Roy, S. Chatterjee, A. Bauza, A. Frontera, S. Chattopadhyay, Cryst. Growth Des. **19**, 5869–5881 (2019)

82. S. Mirdya, A. Frontera, S. Chattopadhyay, CrystEngComm **21**, 6859–6868 (2019)

83. D.J. Majumdar, Y. Agrawal, R. Thomas, Z. Ullah, M.K. Santra, S. Das, T.K. Pal, K. Bankura, D. Mishra, Appl. Organomet. Chem. **34**, e5269 (2020)

84. D.J. Majumdar, T.K. Pal, S.A. Sakib, S. Das, K. Bankura, D. Mishra, Inorg. Chem. Commun. **128**, 108609 (2021)

85. I. Mondal, S. Chatterjee, S. Chattopadhyay, Polyhedron **190**, 114735 (2020)

86. M. Maiti, S. Thakurta, D. Sadhukhan, G. Pilet, G.M. Rosair, A. Nonat, L.J. Charbonniere, S. Mitra, Polyhedron **65**, 6–15 (2013)

87. A.B.P. Lever, *Inorganic Spectroscopy*, 2nd edn. (Elsevier, New York, 1984)

88. L.K. Das, M.G.B. Drew, A. Ghosh, Inorg. Chim. Acta. **394**, 247–254 (2013)

89. D.K. Mishra, U.K. Singha, A. Das, S. Dutta, P. Kar, A. Chakraborty, A. Sen, B. Sinha, J. Coord. Chem. **71**, 2165–2182 (2018)

90. D. Sadhukhan, A. Ray, G. Rosair, L. Charbonnière, S. Mitra, BCSJ **84**, 211–217 (2011)

91. M. Amirnasr, K.J. Schenk, M. Salavati, S. Dehghanpour, A. Taeb, A. Tadjarodi, J. Coord. Chem. **56**, 231–243 (2003)

92. R.G. Pearson, Hard and soft acids and bases. J. Am. Chem. Soc. **85**(22), 3533–3539 (1963)

93. S. Roy, M.G.B. Drew, A. Bauza, A. Frontera, S. Chattopadhyay, New J. Chem. **42**, 6062–6076 (2018)

94. S. Ghosh, P. Chopra, S. Wategaonkar, Phys. Chem. Chem. Phys. **22**(31), 17482–17493 (2020)

95. A. W. Addison, T. N. Rao, J. Reedijk, J. V. Rijn, G. C. Verschoor, J. Chem. Soc. Dalton Trans. 1349−1356 (1984)

96. J.J. McKinnon, D. Jayatilaka, M.A. Spackman, Chem. Commun. **37**, 3814–3816 (2007)

97. C.F. Mackenzie, P.R. Spackman, D. Jayatilaka, M.A. Packman, IUCrJ **4**(5), 575–587 (2017)

98. N. Abad, H. Lgaz, Z. Atioglu, M. Akkurt, J.T. Mague, I.H. Ali, Y. Ramli, J. Mol. Struct. **1221**, 128727 (2020)

99. M.A. Spackman, J.J. McKinnon, D. Jayatilaka, CrystEngComm **10**(4), 377–388 (2008)

100. D. Jayatilaka, D. J. Grimwood, A. Lee, A. Lemay, A. J. Russel, C. Taylor, A. Whitton, TONTO-A System for Computational Chemistry (2005)

101. N. Kanagathara, F. MaryAnjalin, V. Ragavendran, D. Dhanasekaran, R. Usha, R.G.S. Rao, M.K. Marchewka, J. Mol. Struct. **1223**, 128965 (2021)

102. E. Önem, B. Tüzün, S. Akkoç, J. Biomol. Struct. Dyn. 1–12 (2021)

103. B. Tüzün, J. Bhawsar, Arab. J. Chem. **14**(2), 102927 (2021)

104. A. Aktaş A., B. Tüzün, R. Aslan, K. Sayin, H. Ataseven, J. Biomol. Struct. Dyn. 1–11 (2020)

105. A. Poustforoosh, H. Hashemipour, B. Tüzün, A. Pardakhty, M. Mehrabani, M.H. Nematollahi, Biophys. Chem. **272**, 106564 (2021)

106. Adasme et al. PLIP 2021: expanding the scope of the protein–ligand interaction profiler to DNA and RNA. NAR (2021)

107. S.D. Bella, I.P. Oliveri, A. Colombo, C. Dragonetti, S. Righettob, D. Roberto, Dalton Trans. **41**, 7013 (2012)

108. L. Chen, C. Yan, B. Du, K. Wu, L.-Z. Zhang, S.-Y. Yin, M. Pan, Inorg. Chem. Commun. **47**, 13–16 (2014)

109. A. Fashina, T. Nyokong, J. Lumin. **167**, 71–79 (2015)

110. Y. Tang, M. Kong, X. Tian, J. Wang, Q. Xie, A. Wang, Q. Zhang, H. Zhou, J. Wua, Y. Tiana, J. Matter. Chem. B. **5**, 6348–6355 (2017)

Publisher's Note Springer Nature remains neutral with regard to jurisdictional claims in published maps and institutional affiliations.